PHOTONIC SENSORS / Vol. 16, No. 1, 2026: 9560001

Three-Component Distributed Acoustic/Seismic Sensing

Qiang JING[1], Yunjiang RAO[1,2*], Rong TANG[1], Sidan YU[1], Qiyun ZHANG[1], Jiahao WANG[1], Tianyuan YANG[1], Lingfeng MENG[1], Sijin ZHENG[1], Junhang WANG[1], Shengtao ZOU[1], Zhaoyu LI[1], Zengling RAN[1,2], Shujie AN[2], Fengyu TAN[2], Yong SUN[2], Gang YU[2,3], and Haolin CHEN[3]

[1]*Key Laboratory of Optical Fiber Sensing & Communications (Ministry of Education of the People's Republic of China), University of Electronic Science and Technology of China, Chengdu 611731, China*

[2]*Optical Science & Technology (Chengdu) Co., Ltd., Chengdu 611731, China*

[3]*Bureau of Geophysical Prospecting Inc., China National Petroleum Corporation, Zhuozhou 072750, China*

[*]Corresponding author: Yunjiang RAO E-mail: yjrao@uestc.edu.cn

Abstract: Fiber-optic distributed acoustic sensing (DAS) has become a revolutionary technology in the field of acoustic/seismic wave detection as it has disruptive advantages over point acoustic/seismic sensors. Especially, DAS has found vital applications in oil/gas exploration and development. However, three-component DAS (3C-DAS) remains an unsolved bottleneck problem as the present DAS is only sensitive to the axial strain, limiting the application range of DAS greatly. Here, we proposed and verified the 3C-DAS concept based on the theory proposed. We processed signals from three independent optical fibers within a specially designed dual-sine-structured sensing cable to realize 3C-DAS. Field trials of the 3C-DAS units were completed outdoor and in the real oilfield, respectively, by using an ultra-sensitive DAS instrument developed. Furthermore, a 100 m-long 3C-DAS cable was designed, fabricated, and tested. The experimental results indicate that 3C-DAS has the statistically comparable signal-to-noise ratio and better imaging resolution due to higher spatial density when compared to electronic 3C geophones. This work pioneers the study of 3C-DAS and paves a way to develop a new generation of vector DAS systems, including 3C-DAS-based geophones, hydrophones, and sonars for imaging geophysical structures with higher fineness, detecting undersea targets with better resolution, and positioning aerial vehicles with higher accuracy.

Keywords: Distributed acoustic sensing; three-component distributed seismic sensing; optical fiber sensor.

Citation: Qiang JING, Yunjiang RAO, Rong TANG, Sidan YU, Qiyun ZHANG, Jiahao WANG, *et al*., "Three-Component Distributed Acoustic/Seismic Sensing," *Photonic Sensors*, 2026, 16(1): 9560001.

1. Introduction

Dense sensor networks are transforming our understanding of the world through high-resolution environmental monitoring [1]. Point acoustic/seismic sensors are one of the most important types of physical sensors [2–5]. Emerging as a new generation of the dense acoustic/seismic sensing technology, distributed acoustic sensing (DAS) offers substantial advantages over the conventional point sensors, including the large scale, high density, long distance, low cost, easy laying,

Received: 9 October 2025 / Revised: 24 November 2025

DOI: 10.26599/PhoS.2026.9560001
Article type: Research article

and robust survivability [6, 7]. Consequently, DAS has created significant advances for our observation of the world through vibration and sound [8–11]. Cutting-edge DAS can convert optical fibers into extremely dense sensing arrays, enabling acoustic/seismic data acquisition with high sensitivity reaching down to the $p\varepsilon/\sqrt{\text{Hz}}$ level [12, 13], the broad frequency ranges from millihertz to kilohertz [14–16], long sensing distance up to 100 kilometers [17–19], and sub-meter spatial resolution [20, 21]. DAS further demonstrates robust deployment capabilities in harsh environments where the use of the conventional acoustic/seismic sensors is quite hard, such as deep underground with both high temperature and high pressure [22]. Notably, DAS can convert existing telecommunication optical fibers into installation-free sensing networks for regional earthquake monitoring [8, 23–25], near-surface characterization [26, 27], infrastructure safety assessment [28, 29], and marine activities or disasters monitoring [11, 30–32]. Beyond this, DAS can provide solutions for distributed hydroacoustic sensing based on customized cables [10, 33, 34]. Particularly, DAS applications in the borehole have been recognized as a revolutionary shift in oil/gas exploration and development, where DAS is potential to replace the conventional geophones by delivering outstanding advantages: full well coverage, higher spatial resolution, higher operational efficiency, significant cost reduction, and superior downhole survivability [35–37]. Since the first vertical seismic profile (VSP) survey [38], DAS applications in the borehole have expanded rapidly to reservoir monitoring, hydraulic fracturing monitoring, geological structure imaging, mineral exploration, and other areas [6]. The massive acoustic/seismic datasets from DAS recordings further help to drive intelligent oil/gas field optimization and enhance production efficiency and resource management [39, 40]. Despite these extensive deployments, unidirectionality remains a fundamental and primary constraint on DAS applications. This restriction originates from the operating principle of current single-component DAS, where the optical fiber is just sensitive to the axial strain [41].

High-resolution seismic imaging and accurate subsurface characterization necessitate the detection of the three mutually perpendicular components [39], since the subsurface structures are revealed by analyzing different polarizations of seismic waves propagating through the Earth's layers with compressional and shear motions [43]. Generally speaking, electronic three-component (3C) geophone arrays have been widely used, while optical fiber-based point 3C sensors offer alternative options but are greatly restricted by the limited capacity and high cost [44, 45]. In principle, DAS directionality may be realized partially by changing cable installation strategies or by designing the geometric distribution of fibers within the cable dimension. The combinations of the surface and VSP data [46, 47], and loop arrays [48] have been reported, but their deployment complexity and high operational costs make them impractical. Helically wound cables (HWC) can obtain the 3C information [49–51], but the separation of the overlapped 3C signal from DAS data remains fundamentally challenging and has not yet been really realized. The assumptions of non-standard spatial patterns of optical fibers (serpentine, looped, sinusoidal shapes, etc.) have been proposed to enhance DAS directional sensitivity and enable 3C separation [52], yet these assumptions are purely qualitative and remain unrealized.

In this study, we proposed the concept of 3C-DAS and achieved fully-distributed 3C seismic detection, for the first time, based on the combination of two sinusoidally arranged optical fibers and one straight optical fiber integrated on an elastic cable. The theory of 3C-DAS was presented to guide the design of the 3C-DAS cable. The acquisition of 3C-DAS signals with an ultra-sensitive DAS instrument (uDAS) was carried out and its responses correlated well with co-located 3C electronic geophones, hence verifying the concept of the 3C-DAS proposed. Furthermore, fully-distributed 3C data were recorded by using a 100-meter-long 3C-DAS cable fabricated to characterize the near-surface structure of the ground via inversion of surface seismic waves. The high-density spatial samplings of 3C-DAS can provide superior inversion resolution with the higher efficiency and lower cost when compared to 3C electronic geophones. Real field trials collaborated closely with industry show that 3C seismic recordings obtained with uDAS enable finer seismic imaging. In particular, in horizontal land deployments where single-component DAS fails to capture critical wave modes, the 3C-DAS can resolve reflected seismic waves, enabling high-resolution imaging of stratigraphic boundaries previously undetectable with single-component DAS. Such a 3C-DAS method would provide a revolutionary way to realize fully-distributed 3C seismic imaging in well-ground or well-sea jointed acquisitions, as shown in Figs. 1(a) and 1(b).

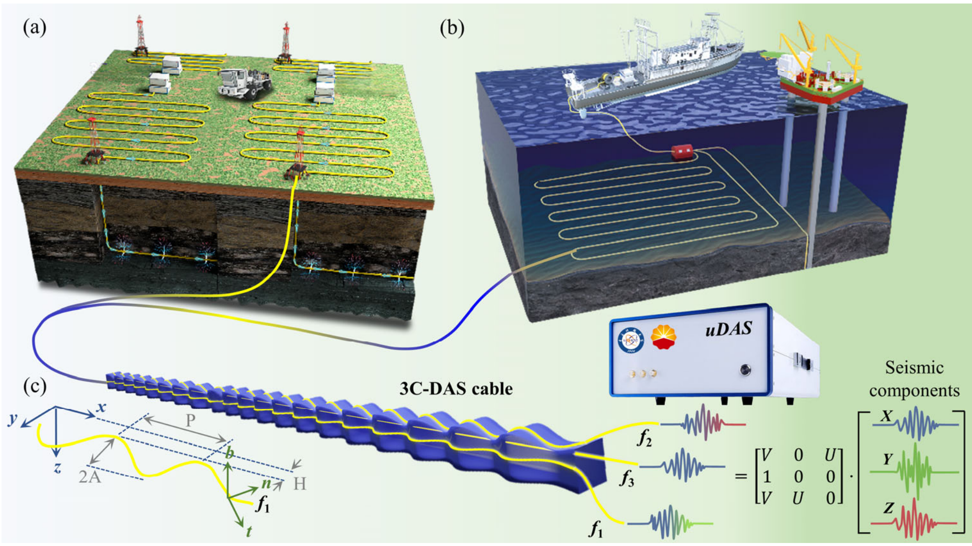

Fig. 1 Concept of 3C-DAS: (a) potential applications of 3C-DAS to ground and downhole oil/gas exploration by using well-ground or well-sea jointed acquisitions, (b) potential applications of 3C-DAS to underwater acoustic/seismic detection, and (c) conceptual diagram of the 3C-DAS cable with the uDAS instrument.

2. Concept of 3C-DAS

Acoustic disturbances induce the axial strain in optical fibers, modulating the phase of propagating optical pulses. DAS samples the continuous Rayleigh backscattering light of the fiber and extracts the phase information from optical intensity. At the location indexed by s_0 along the fiber, the phase $\varphi(s_0)$ is not linear to the strain. However, the phase difference $\varphi(s_0+L)-\varphi(s_0)$ is proportional to the average strain of the fiber section s_0~s_0+L. A sensing array with dense channels is obtained after phase differentiation. The channel center is indexed by $s_0+L/2$. Here, the length L is also known as the gauge length. Since these phase changes are proportional to the axial strain, the responses of DAS to different seismic components are mainly determined by fiber geometry [53]. Here, 3C-DAS uses a multi-fiber configuration with dual sinusoidally arranged fibers (SAFs) and a straight fiber [Fig. 1(c)]. The SAFs are distributed on two orthogonal planes along an elastic cable, while the straight fiber is arranged along the cable axis. The seismic event produces three orthogonal vibration signals due to the coupling of waves with different polarizations. The straight fiber is only sensitive to the axial strain, i.e., the X component of the seismic signal. The periodic variation of the fiber tangential vector enables the SAFs to acquire more comprehensive information from radial components, i.e., Y and Z components. Reconstruction of the 3C seismic signal is achieved by the projection of DAS responses from these fibers through the rotation matrix shown in Fig. 1(c).

3. Theory of 3C-DAS

In the concept of 3C-DAS shown in Fig. 1(c), a ground coordinate system ($\mathbf{x}$, $\mathbf{y}$, $\mathbf{z}$) with invariant axis orientations is defined to analyze the responses of optical fibers to strains induced by seismic waves. The fiber's local Frenet-Serret coordinate system is defined by the orthogonal unit vectors [$\mathbf{t}(s)$, $\mathbf{n}(s)$, $\mathbf{b}(s)$], representing the tangential, normal, and binormal directions at the position s along the fiber, respectively. To model DAS data, the strain tensor must be transformed from ground to fiber coordinates. The projection of the instantaneous strain tensor can be accomplished via coordinate transformations $\varepsilon_{nbt}(s)=\mathbf{G}(s)\varepsilon_{xyz}\mathbf{G}^{\mathrm{T}}(s)$, where $\mathbf{G}(s)$ is the rotation matrix along a fiber distance s:

$$\mathbf{G}(s)=\begin{bmatrix}\mathbf{n}(s)\cdot\mathbf{x} & \mathbf{n}(s)\cdot\mathbf{y} & \mathbf{n}(s)\cdot\mathbf{z}\\ \mathbf{b}(s)\cdot\mathbf{x} & \mathbf{b}(s)\cdot\mathbf{y} & \mathbf{b}(s)\cdot\mathbf{z}\\ \mathbf{t}(s)\cdot\mathbf{x} & \mathbf{t}(s)\cdot\mathbf{y} & \mathbf{t}(s)\cdot\mathbf{z}\end{bmatrix}. \tag{1}$$

ε_{xyz} is the strain tensor with six components ε_{ij} (i, j=x, y, z). It is defined in the ground coordinate system, not along the seismic ray path. The fiber strain can be regarded as a secondary projection of the seismic strain from ray-based to fiber-local coordinates. Both DAS and geophone measurements capture one or more orthogonal seismic components. Before further analysis, we adopt these assumptions. 1) The cable interacts with plane waves at wavelengths much larger than the cable radius, so that the torsion induced strain is negligible [49]. 2) The seismic wavefield strain remains uniform across the DAS interrogation gauge length, so the instantaneous strain tensor ε_{xyz} is constant over the studied gauge length. For example, gauge lengths below 5 m are appropriate for resolving frequencies above 50 Hz, assuming seismic velocities of 0.8 km/s–5 km/s, as the wavelength should be at least 3 times–5 times of the gauge length. 3) The tight combination between the cable and the ground ensures reliable strain transfer. Then, the transformed fiber axial strain is expressed as

$$\begin{aligned}\varepsilon_{tt}(s)=&\left[\mathbf{t}(s)\cdot\mathbf{x}\right]^2\varepsilon_{xx}+\left[\mathbf{t}(s)\cdot\mathbf{y}\right]^2\varepsilon_{yy}+\left[\mathbf{t}(s)\cdot\mathbf{z}\right]^2\varepsilon_{zz}+\\ &2\left[\mathbf{t}(s)\cdot\mathbf{x}\right]\left[\mathbf{t}(s)\cdot\mathbf{y}\right]\varepsilon_{xy}+2\left[\mathbf{t}(s)\cdot\mathbf{x}\right]\left[\mathbf{t}(s)\cdot\mathbf{z}\right]\varepsilon_{xz}+\\ &2\left[\mathbf{t}(s)\cdot\mathbf{y}\right]\left[\mathbf{t}(s)\cdot\mathbf{z}\right]\varepsilon_{yz}.\end{aligned} \tag{2}$$

For straight fibers used in VSP surveys, the vertical cable orientation yields the axial strain $\varepsilon_{tt}(s)$=ε_{zz}. DAS data represent the average strain within one gauge length along the cable. When primary waves propagate at the angle θ to the fiber axis, DAS sensitivity exhibits a $\cos^2\theta$ dependence on the incidence direction [41]. For shaped fibers, the averaged strain over the gauge length is calculated by the integration of the local tangential strain over an integer multiple of the fiber's winding period, $\int_{s_0}^{s_0+L}\varepsilon_{tt}(s)\mathrm{d}s/L$. This spatial integrability is attributed to the periodic distribution of the wrapped fibers. However, the three-dimensional winding geometry in ground coordinates increases the complexity of stain projection. Furthermore, in order to obtain a well-conditioned rotation matrix, additional optimization of the winding geometry is required [51]. Here, we propose the multi-fiber configuration with the SAFs and straight fiber, as shown in Fig. 1(c). For the fiber f_1 distributed in the xoy plane, the transformed tangential strain is written as

$$\begin{aligned}\varepsilon_{tt}^{f_1}(s)=&\left[\mathbf{t}(s)\cdot\mathbf{x}\right]^2\varepsilon_{xx}+\left[\mathbf{t}(s)\cdot\mathbf{y}\right]^2\varepsilon_{yy}+\\ &2\left[\mathbf{t}(s)\cdot\mathbf{x}\right]\left[\mathbf{t}(s)\cdot\mathbf{y}\right]\varepsilon_{xy}.\end{aligned} \tag{3}$$

The geometry of fiber f_1 is given by the following relations:

$$\begin{cases}y=H+A\sin(2\pi x/P)\\ z=\text{const.}\end{cases} \tag{4}$$

where H is the y-axis offset; A and P are the amplitude and period of the sinusoidal function, respectively. Then, (3) can be expressed as

$$\varepsilon_{tt}^{f_1}(x)=\frac{\eta^2}{1+\eta^2}\varepsilon_{yy}+\frac{1}{1+\eta^2}\varepsilon_{xx}+\frac{2\eta}{1+\eta^2}\varepsilon_{xy} \quad (5)$$

with η=cos(2$\pi x/P$)·2$\pi A/P$. Considering the integration of the local tangential strain over an integer multiple of the sinusoidal period, the averaged fiber strain over the gauge length L is

$$\frac{1}{L}\int_{nP}\varepsilon_{tt}^{f_1}(x)\mathrm{d}x=\frac{\varepsilon_{yy}}{L}\int_{nP}\frac{\eta^2}{1+\eta^2}\mathrm{d}x+\frac{\varepsilon_{xx}}{L}\int_{nP}\frac{1}{1+\eta^2}\mathrm{d}y \quad (6)$$

where the third term in (5) vanishes after integration. We write the scaling factors of ε_{yy} and ε_{xx} as $U(P/A)$ and $V(P/A)$, which are the functions of period-amplitude-ratio. For the fiber f_2 which has the same geometry as f_1 but is assembled in the xoz plane, the averaged fiber strain becomes

$$\frac{1}{L}\int_{nP}\varepsilon_{tt}^{f_2}(x)\mathrm{d}x=U\varepsilon_{zz}+V\varepsilon_{xx}\,. \quad (7)$$

As a result, the quantitative relationship between the DAS measurement and the ground strain components is given by

$$\begin{bmatrix}\varepsilon_{\mathrm{DAS}}^{f_1}\\ \varepsilon_{\mathrm{DAS}}^{f_2}\\ \varepsilon_{\mathrm{DAS}}^{f_3}\end{bmatrix}=\begin{bmatrix}V & U & 0\\ V & 0 & U\\ 1 & 0 & 0\end{bmatrix}\begin{bmatrix}\varepsilon_{xx}\\ \varepsilon_{yy}\\ \varepsilon_{zz}\end{bmatrix}. \quad (8)$$

Although the analytical expressions of the scaling factors U and V are complicated, we can calculate the numerical results for the specific period-amplitude-ratio with P/A= 3.63. The scaling factors of SAFs to ground strain components are equal in value (see Supplementary files S1).

4. Concept verification with a single 3C-DAS unit

A single sensing unit with a meter-scale length was first fabricated to validate the 3C-DAS theory proposed. We first fabricated an elastomer with surface grooves using a dedicated mould and pre-applied an adhesive layer. The fibers were then pressed into the grooves with a controlled pre-tension using rigid inserts shaped to match the elastomer surface precisely. Once the fibers were fully seated within the grooves, the curing process was performed to secure and protect it. Finally, the entire sensing unit was protected with an additional reinforcing layer.

We buried the sensing unit with rammed backfill, and deployed a co-located 3C electronic geophone (Geolight GL-CS60, China) for comparison. The seismic signal was generated by a 10 kg free-falling weight. The strains of the fibers were obtained with a 10 m gauge length using a uDAS instrument developed [54]. This instrument provides temporal-spatial two-dimensional strain data, and each column (channel) of the data is equivalent to the temporal waveform of one geophone, with no overlap between gauges recorded. The channel spacing of 0.4 m enables much denser spatial sampling over the geophones for enhancing horizontal resolution in imaging. The time division multiplexing (TDM) method was employed for interrogation (see Supplementary files S2). Three sensing fibers were installed in series without splices, with desensitized fiber segments exceeding twice the gauge length to avoid channel crosstalk. For each sensing fiber, the central channel within the disturbed section was selected as the representative output. Subsequently, these fiber strain measurements were converted into 3C ground strains through the rotation matrix given by (8).

The conventional geophones are sensitive to the particle velocity of the point where they are fixed, while the uDAS instrument used provides an averaged strain measurement over the gauge length. For the DAS instrument providing strain rate outputs, the conversion is done by rescaling time-integrated DAS data [22], applying a two-spatial averaging filter [55], or integrating DAS data in space [56]. The direct comparison between the geophone and DAS data from the straight fiber is realized employing these methods. Here, we rescaled uDAS strain data to the equivalent particle velocity for comparison with geophone measurements. This conversion relies on the theoretical relationship for plane seismic waves [22], where the ratio between the particle velocity $v_x=\partial u/\partial t$ and strain $\varepsilon_{xx}=\partial u/\partial x$ is given by the apparent velocity $c=\pm v/\varepsilon$ and $u(x, t)$ denotes the dynamic displacement.

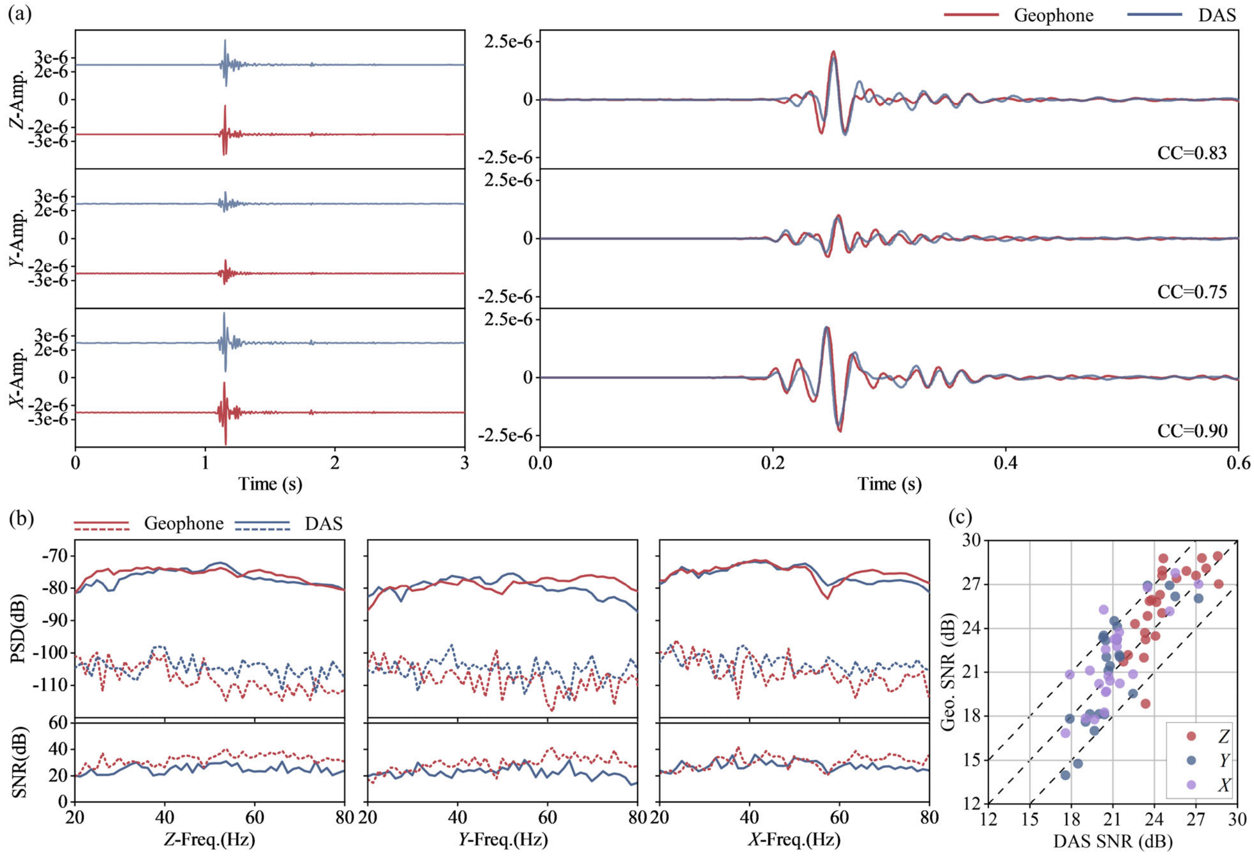

Fig. 2 Test results of the sensing units: (a) the waveforms of one shot [the first and second columns show the 3C waveforms and normalized waveforms of DAS (blue) and geophone (red), and the DAS waveforms in the first column are scaled to match the peaks of geophone waveforms, (b) the top row showing the PSD of the signal and noise in (a) from DAS (blue) and geophone (red) and the bottom row plotting the PSD difference, and (c) the temporal SNR of 3C data recorded by the DAS and geophone (the dashed lines show ratios of 0.5, 1, and 2 for reference) (Amp.: amplitude; Freq.: frequency; Geo.: geophone; CC: cross-correlation coefficient; SNR: signal-to-noise ratio).

We conducted the test at the campus of University of Electronic Science and Technology of China (UESTC). The waveforms of DAS and 3C geophones at a shot-receiver distance of 10 m with an orientation of 45°, are plotted in Fig. 2(a). In the left column, the DAS record is scaled to match its root-mean-square (RMS) amplitude in 3 s with that of the geophone, and the waveforms are offset vertically for clarity. The right column shows time-aligned normalized waveforms in 1 s using cross-correlation time shifts. The CCs within the 3 s window indicate good consistency. In Fig. 2(b), the power spectral density (PSD) diagrams of the noise and seismic signal are calculated within 0.8 s windows before and after the first arrival. DAS exhibits the similar frequency contents and comparable SNR to the geophone. The coupling and locally scattered signals induced by small-scale heterogeneity near the surface may contribute to the difference in the waveforms of the DAS and co-located geophone. The temporal SNR is calculated by the RMS amplitude ratio of the signal and noise in a window before and after the first arrival. The temporal SNR of shots selected from

8 source locations oriented at 45° intervals is illustrated in Fig. 2(c). The results demonstrate comparable SNRs between DAS and geophone measurements. For some shots, the horizontal components of DAS measurements exhibit up to a two-fold SNR enhancement relative to the geophone, while the vertical component shows the approximately 50% lower SNR. This may be related to the coupling as well as the polarization of the seismic waves. The test of the 3C sensing unit shows that the proposed configuration effectively detects multicomponent seismic signals and is able to extract 3C signals from the SAFs and straight fiber. DAS demonstrates good consistency in waveforms and statistically comparable SNRs to geophone signals.

5. Real field trial of the 3C-DAS unit

We tested the sensing units at a real 3D seismic exploration site in Jiangyou, Sichuan province, China and compared their waveforms with 3C geophones (Sercel DSU3, France) used in hydrocarbon production sites by collaborating with Bureau of Geophysical Prospecting Inc., China, which has maintained the largest business scale in the global industry of oil/gas exploration for ten consecutive years. As illustrated in Fig. 3(a), the DAS line (yellow) with 26 sensing units was deployed alongside the geophone line (blue) with 10 DAS sensing units picked and indexed by yellow dots. The geophones were placed at intervals of 40 m, while the sensing units fabricated in series were distributed at non-uniform intervals due to practical terrain constraints. The seismic waves were generated by explosives in a well.

Two types of sensors simultaneously recorded seismic signals from the single shot and their filtered recordings at the source location S1 are plotted in Figs. 3(b)–3(g). Both direct and reflected waves were recorded in the vertical component of the DAS [Fig. 3(b)] and geophone [Fig. 3(c)]. As illustrated in Figs. 3(d)–3(g), reflected waves show negligible visibility in the X component and weak visibility in the Y component for both DAS and geophone recordings. Horizontal single-component DAS deployments exclusively detected X component seismic energy and showed no observable reflected waves [similar to Fig. 3(d)]. Surface waves were not recorded due to the limited array length and the source-receivers location. The waveforms at U1 are plotted in Fig. 3(h), the geophone data are rescaled to the equivalent nanostrain by the RMS amplitude ratio of direct waves in the vertical component, 4 358 m/s. It is close to the apparent velocity 4 500 m/s obtained from the moveout. The waveforms of DAS and geophones demonstrate good consistency due to a more homogeneous seismic wavefield under a kilometer-scale shot-receiver distance when compared to normal outdoor tests with the limited distance. The PSD diagrams illustrated in Fig. 3(i) show good consistency in the distribution of the spectral energy between the two sensors.

We estimated the temporal SNR by comparing the RMS amplitude ratio in a 2 s window of the signal and noise. The temporal SNR of the DAS and geophone from S1 was calculated and shown in Fig. 3(j). The SNR decreased with the extended source-receiver distance and the low SNR point near 4.2 km was caused by the environment where sensors were deployed. The lower SNR in the vertical component of DAS may be attributed to coupling during the backfilling and compaction and optical losses. The temporal SNR values of U1 from 10 sources are shown in Fig. 3(k), with the source location indexed by black numbers in the data points. DAS exhibited the statistically comparable SNR to that of the geophone within the 3 dB range. Additional waveforms are provided in Supplementary files S3.

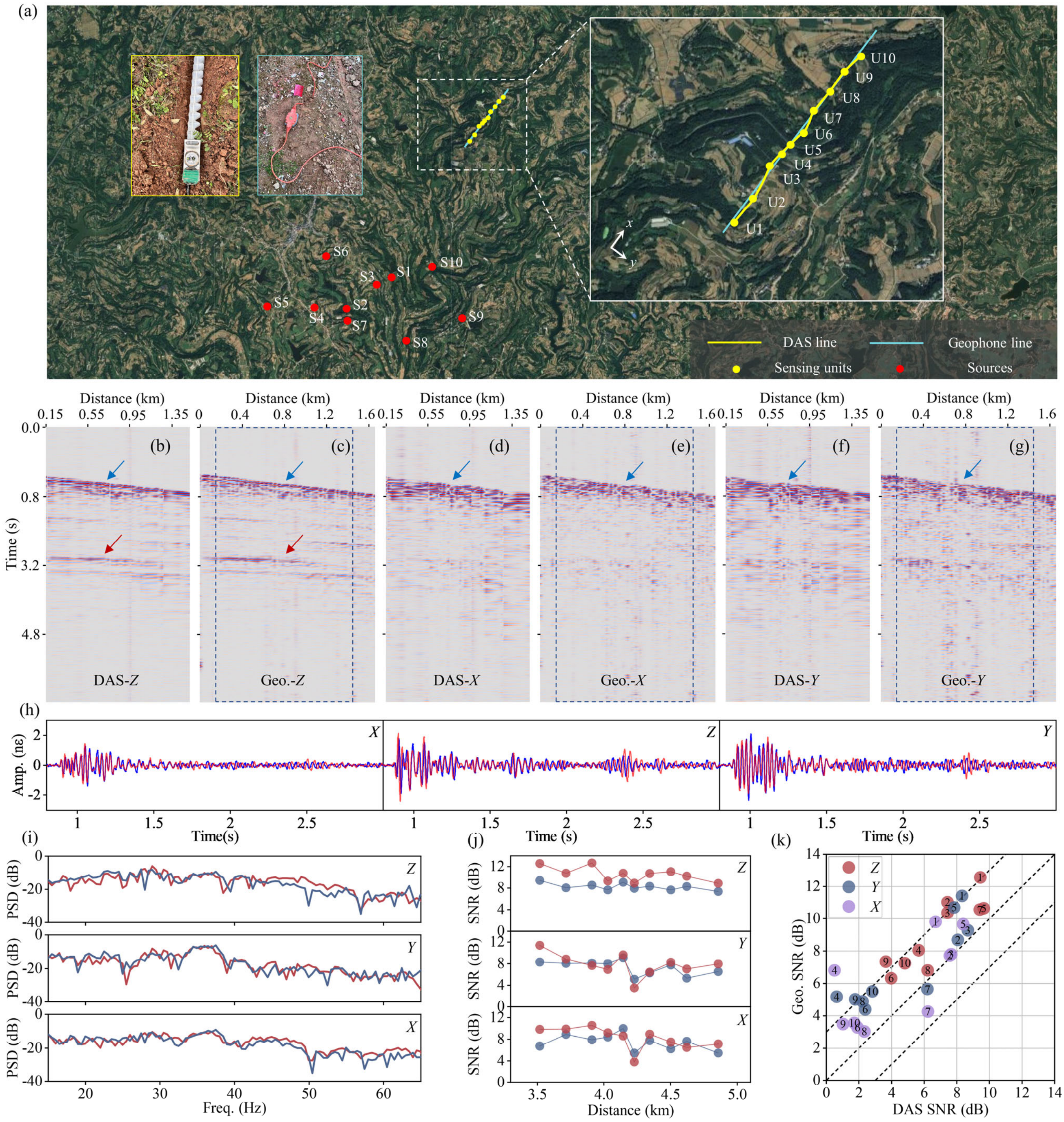

Fig. 3 Layouts of the field test and the comparison of 3C recordings from sensing units and co-located geophones: (a) the layout of test (the insets show the pictures of the sensing unit and geophone), (b) and (c) are the recordings of the *Z* component from the DAS and geophone under S1, (d) and (e) are the recordings of the *X* component, (f) and (g) are the recordings of the *Y* component [the blue and red arrows indicate the direct wave and reflected wave, respectively; the blue dashed boxes in (c), (e), and (g) indicate the corresponding DAS data ranges], (h) the 3C waveforms of the DAS (blue) and geophones (red) at U1 under S1, (i) the PSD of the DAS (blue) and geophone (red) signals in (h), (j) the temporal SNR of the DAS (blue) and geophone (red) of U1–U10 from S1, and (k) the temporal SNR at U1 from ten source locations (the dashed lines show ratios of 0.5, 1, and 2 for reference).

6. Field trial of fully-distributed 3C seismic sensing

The trial was conducted at the campus of UESTC. As shown in Fig. 4(a), a 100 m-long distributed sensing cable was fabricated and installed in a surface trench with the rammed backfill. The continuous sensing cable used in this trial was assembled by concatenating multiple sensing units. The cable deployment started at the location B and ended at D. Ten co-located 3C geophone channels (spaced at 10 m intervals) were obtained by repeatedly deploying two geophones along the cable.

Two segments of SAFs f_1 and f_2, and one straight fiber f_3 were carefully assembled and spliced in series. This TDM method has been demonstrated to have no effect on signal quality at the back end of the link (extended data in Fig. S7 of the Supplementary files). The time delay of the co-located DAS channels from three fibers could be neglected, given that the repetition rate of the laser pulse was significantly greater than the seismic frequency of interest. In this trial, seismic waves were generated by a 10 kg free-falling weight from a height of 1.5 m. Three source locations (S1–S3) were arranged, at distances of 20 m, 50 m, and 80 m from the point B, respectively. A lateral offset of 10 m was adopted to obtain a more uniform seismic wavefield at the nearest DAS channels to the shot location.

An example shot recorded by uDAS at the source location S2 is shown in Fig. 4(b). After normalization, the visibility of low-amplitude signals can be enhanced for better detecting the moveout on seismic waves. For each source location, the DAS recordings from five shots were synchronized through cross-correlation and subsequently stacked. The raw phase data of uDAS were converted to the strain, which was in phase with the velocity. uDAS provided a dense spatial sampling of 124 channels with the 0.8 m spacing and 5 m gauge length. The primary wave was the first arriving coherent energy, followed by the dominant seismic energy contributed by the ground roll of the Rayleigh wave, which was clearly visible in the 3C recordings. Some visible energy in the Rayleigh wave coda might be induced by wave interference. In the left panel of Fig. 4(b), the waveforms were aligned by cross-correlation, which showed good consistency. Compared with the 3C-DAS sensing unit, the continuous sensing cable introduced a larger-scale strain averaging. The variable coupling, wave interference, and inhomogeneity may have a greater impact on waveform similarity. The temporal SNR was calculated as well (extended data in Fig. S12 of the Supplementary files). DAS achieved the statistically comparable SNR to that of the geophone.

The waveforms of the DAS and co-located geophone with a shot-receiver distance of 25 m are plotted in Fig. 4(c). The primary wave was observed clearly in X and Y components, and weakly in the Z component of DAS. The surface wave was detected in three components of the DAS and geophone. The PSD diagrams are plotted in Fig. 4(d), where two sensors had similar spectral components. The fundamental difference between spatially averaged measurements and point sensing led to the response difference between two sensors. Especially for near-surface seismic waves, inhomogeneity and interference are more likely to affect the data quality. We further generated continuous seismic waves with a handheld tamper that provided a stable vibration. We selected a DAS channel at 20 m and placed three shot locations with a distance of 20 m in the x-negative direction from this channel, and two others at offsets of 30 m and 80 m in the x-positive direction. As shown in Fig. 4(e), the tamper maintained in the ignition start state of the initial 0.5 s within a 2 s window, followed by a bouncing motion for the next 1.5 s. It can be found that 3C waveforms of DAS and geophones showed good consistency in phase.

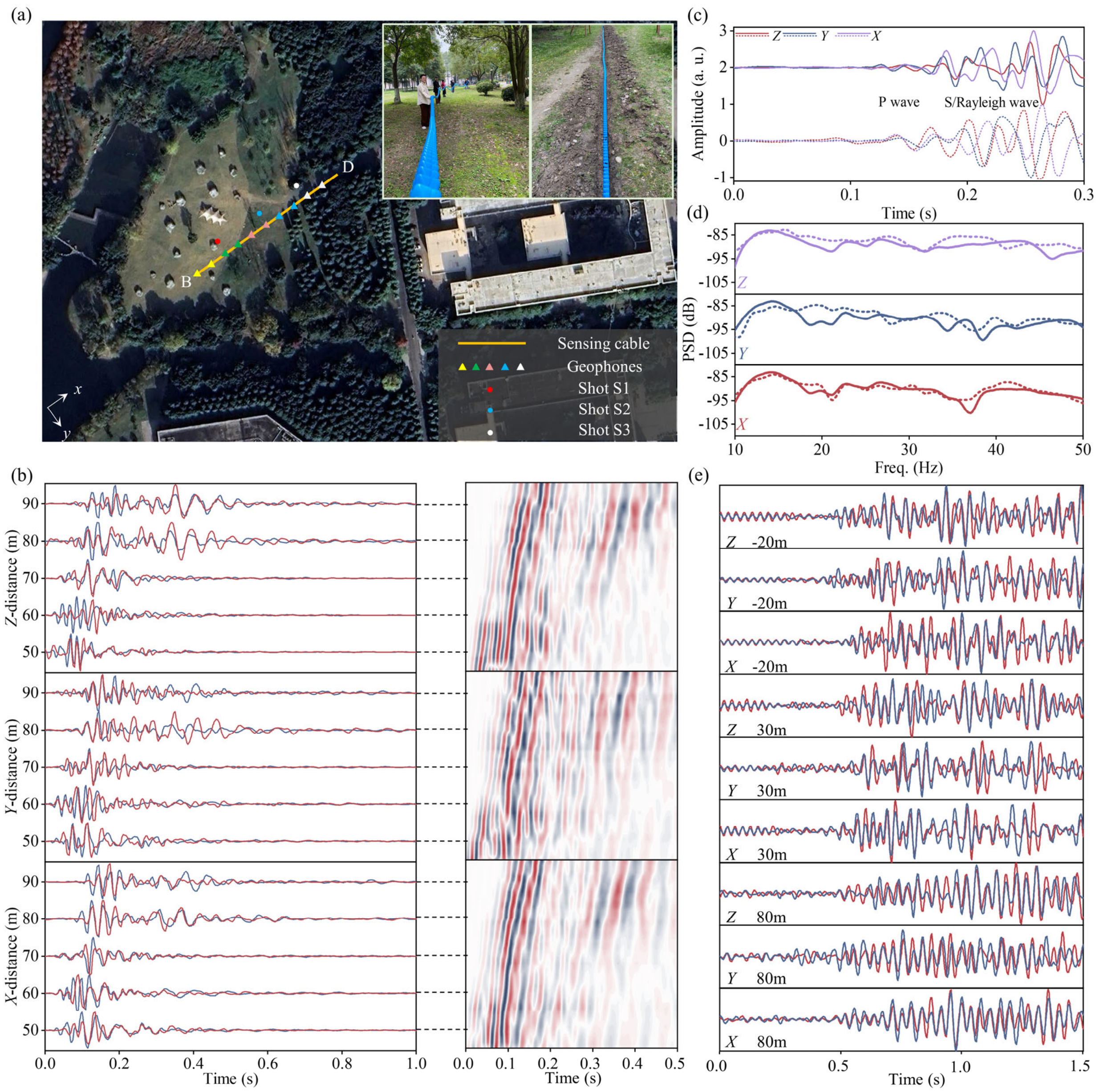

Fig. 4 Layouts of the field trial with fully distributed cable and co-located geophones: (a) the layout with the insets showing the fabricated distributed sensing cable, (b) the 3C recordings of DAS (the right column) and the waveforms of DAS (blue) and co-located geophone (red) in the left column, (c) the DAS (solid) and geophone (dashed) waveforms from S2 at a shot-receiver distance of 25 m, (d) the PSD of the DAS (solid) and geophone (dashed) waveforms in (c), and (e) 3C waveforms of the DAS (blue) and co-located geophone (red) at different shot-receiver distances, with seismic waves generated by a handheld tamper.

7. Surface wave imaging application

We performed multi-channel analysis of surface waves on 3C-DAS recordings to verify the feasibility of adopting 3C-DAS for near-surface geophysical applications. 3C wavefields from the linear cable show surface waves with clear dispersive effects, as shown from the results of one shot under S2 [see Fig. 4(a)] in Figs. 5(a)–5(c) and extended data in Fig. S11 of the supplementary materials. The fundamental and higher order modes were observed while these fundamental modes showed similar shapes. Only the fundamental modes in DAS spectra were picked and inverted due to the unreliability of the higher order modes. The geophone spectra in Figs. 5(d)–5(f) show similar fundamental mode profiles to that of DAS, particularly in the vertical component. The dispersion curve picking from geophones was impeded by the spectral discontinuity and stronger noise. The high-resolution *f*-*v* spectra of DAS showed higher sensitivity with a relatively wide frequency range. For the DAS sensing cable, the spatial sampling interval was 0.8 m, which was 12.5 times denser than that of the geophones. In Figs. 5(a)–5(c), the inverted dispersion curves with red circles closely matched the picked black circles. Thereafter, we obtained the 1-dimensional (1D) shear wave velocity-depth profile from the inversion, as shown in Fig. 5(g).

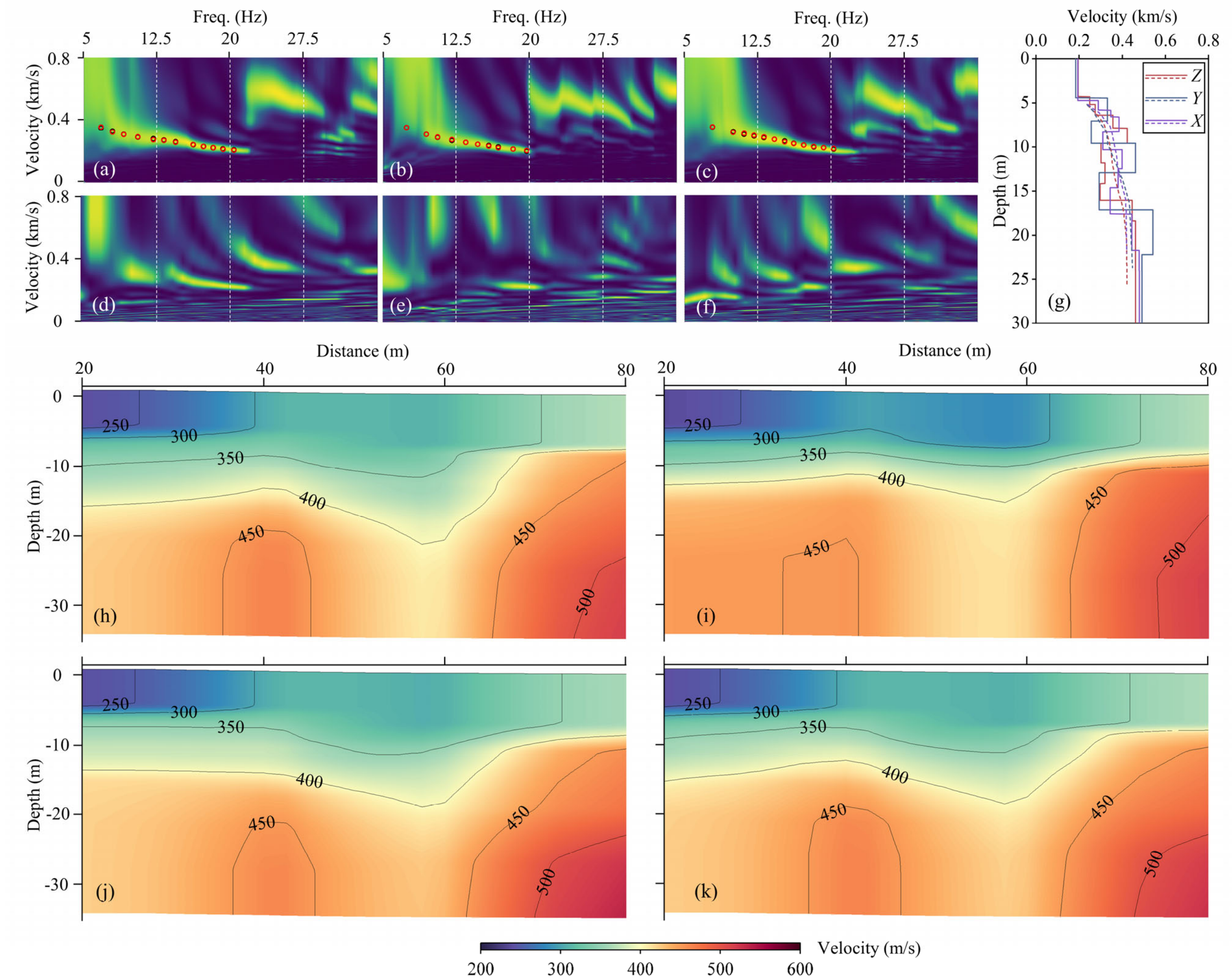

Fig. 5 *f*-*v* spectra and inversion results: *f*-*v* spectra of the components (a) & (d) *Z*, (b) & (e) *Y*, (c) & (f) *X* from the DAS (top row) and co-located geophone (bottom row) are demonstrated (the black and red circles were observed and inverted dispersion curves of DAS), (g) inverted 1D S-wave velocity structures of three components, inverted 2-dimensional (2D) apparent velocity profiles from the components (h) *Z*, (i) *Y*, (j) *X*, and (k) their combinations are plotted as well.

We further gathered the dispersion curves of the shots from S1 to S3 (see Supplementary files S4) to build the 2D inversion profiles from three components and their combination, as shown in Figs. 5(h)–5(k). The final 2D velocity profiles of the three components were quite similar, with a maximum detection depth of 35 m. The profile combined with the three components depicted the velocity layers more accurately. The imaging results indicated that 3C-DAS was an effective way for near-surface characterization.

8. Summary and discussion

Over the course of the past decade, the majority of studies on DAS have been constrained in single-component sensing, particularly in the field of seismic sensing. This presents a significant challenge for further advances in the DAS technology and applications. Our study provides a new approach to achieve real 3C-DAS. The testing results of the 3C-DAS unit show comparable waveforms to 3C electronic geophones in all three components. A fully-distributed sensing cable with a length of 100 m was designed and fabricated to acquire surface 3C-DAS data. The field trial data demonstrate that 3C-DAS is able to provide ultra-high density 3C surface seismic data. The imaging results show that the velocity profiles adequately describe the near-surface structures. This work proves the concept and feasibility of the 3C-DAS well. The elastic dynamics of the 3C-DAS cable remain analytically complicated and can be studied by investigating the mechanical model of the interaction between the sensing fiber and the elastic cable in the near future. In addition, continuous fabrication of kilometer-level-length 3C-DAS cables remains an unsolved engineering problem. Although it is beyond the scope of this study, we provide a possible fabrication method in Supplementary files S1. The sensing range is primarily limited by the DAS interrogator. By using a three-channel uDAS interrogator with a sensing range of 60 km, the maximum sensing range of 3C-DAS is ~39 km considering the length ratio of SAFs to straight fiber (1.54).

In summary, the concept and theory of 3C-DAS were proposed and verified by real field trials, for the first time. 3C-DAS not only provides a novel acoustic sensing method for realizing the dense detection of 3C seismic waves, enabling the observation of finer geological structures, but also offers great potential for the development of a new generation of vector DAS systems for underground, underwater, and airborne applications with better performances. Therefore, this study would significantly expand the application range of DAS due to the fundamental breakthrough from scalar to vector and have a big impact on the advances of the DAS technology and industry. It can be anticipated that 3C-DAS would find wide applications in various areas, including oil/gas exploration and development (3C-geophone array), undersea target detection and recognition (3C-hydrophone array), and unmanned aerial vehicle detection and recognition (3C-sonar array).

Supplementary files

The supplementary files can be downloaded from the webpage of this article in Photonic Sensors (https://www.sciopen.com/journal/1674-9251).

Acknowledgment

This work is supported by the Key Project of Natural Science Foundation of China (Grant No. U21A20453), and the Research & Development Project by Optical Science & Technology (Chengdu) Co., Ltd., China.

Declarations

Conflict of Interest Yunjiang RAO is the editor-in-chief for Photonic Sensors and was not involved in the editorial review, or the decision to publish this article. All authors declare that there are no competing interests.

Permissions All the included figures, tables, or text passages that have already been published elsewhere have obtained the permission from the copyright owner(s) for both the print and online format.

Use of AI Statement None.

References

[1] K. Iniewski, "*Optical, Acoustic, Magnetic, and*

Mechanical Sensor Technologies," Boca Raton: CRC Press, 2017.

[2] S. Maurice, B. Chide, N. Murdoch, R. D. Lorenz, D. Mimoun, R. C. Wiens, *et al*., "In situ recording of Mars soundscape," *Nature*, 2022, 605(7911): 653–658.

[3] E. A. Podolskiy, Y. Murai, N. Kanna, and S. Sugiyama, "Ocean-bottom and surface seismometers reveal continuous glacial tremor and slip," *Nature Communications*, 2021, 12(1): 3929.

[4] X. Cao, H. Yang, Z. L. Wu, and B. B. Li, "Ultrasound sensing with optical microcavities," *Light: Science & Applications*, 2024, 13(1): 159.

[5] F. Zhuang, Y. Li, T. Guo, Q. Yang, Y. Luo, J. Wang, *et al*., "Review on in-situ marine monitoring using physical and chemical optical fiber sensors," *Photonic Sensors*, 2025, 15(2): 250230.

[6] Y. Li, M. Karrenbach, and J. B. Ajo-Franklin, "*Distributed Acoustic Sensing in Geophysics: Methods and Applications*," 1st ed., Hoboken: Wiley, 2021.

[7] B. Shi, D. Zhang, H. Zhu, C. Zhang, K. Gu, H. Sang, *et al*., "DFOS applications to geo-engineering monitoring," *Photonic Sensors*, 2021, 11(2): 158–186.

[8] N. J. Lindsey, T. C. Dawe, and J. B. Ajo-Franklin, "Illuminating seafloor faults and ocean dynamics with dark fiber distributed acoustic sensing," *Science*, 2019, 366(6469): 1103–1107.

[9] N. Lalam, S. Bukka, H. Bhatta, M. Buric, P. Ohodnicki, and R. Wright, "Achieving precise multiparameter measurements with distributed optical fiber sensor using wavelength diversity and deep neural networks," *Communications Engineering*, 2024, 3(1): 121.

[10] C. Caudron, Y. Miao, Z. J. Spica, C. Wollin, C. Haberland, P. Jousset, *et al*., "Monitoring underwater volcano degassing using fiber-optic sensing," *Scientific Reports*, 2024, 14(1): 3128.

[11] J. Li, E. Biondi, E. R. Heimisson, S. Puel, Q. Zhai, S. Zhang, *et al*., "Minute-scale dynamics of recurrent dike intrusions in Iceland with fiber-optic geodesy," *Science*, 2025, 388(6752): 1189–1193.

[12] J. T. Li, B. Chang, J. T. Du, T. Tan, Y. Geng, H. Zhou, *et al*., "Coherently parallel fiber-optic distributed acoustic sensing using dual Kerr soliton microcombs," *Science Advances*, 2024, 10(3): eadf8666.

[13] Z. Cheng, X. Shu, L. Ma, B. Chen, C. Li, C. Sun, *et al*., "On-chip silicon electro-optical modulator with ultra-high extinction ratio for fiber-optic distributed acoustic sensing," *Nature Communications*, 2023, 14(1): 7409.

[14] G. Gagliardi, M. Salza, S. Avino, P. Ferraro, and P. De Natale, "Probing the ultimate limit of fiber-optic strain sensing," *Science*, 2010, 330(6007): 1081–1084.

[15] J. Jiang, Z. Wang, Z. Wang, Z. Qiu, C. Liu, and Y. Rao, "Continuous chirped-wave phase-sensitive optical time domain reflectometry," *Optics Letters*, 2021, 46(3): 685.

[16] Y. Deng, Q. Liu, and Z. He, "Distributed fiber-optic acoustic sensor for sparse-wideband vibration sensing with time delay sampling," *IEEE Sensors Journal*, 2021, 21(12): 13290–13295.

[17] J. Li, T. Kim, N. Lapusta, E. Biondi, and Z. Zhan, "The break of earthquake asperities imaged by distributed acoustic sensing," *Nature*, 2023, 620(7975): 800–806.

[18] Z. N. Wang, J. J. Zeng, J. Li, M. Q. Fan, H. Wu, F. Peng, *et al*., "Ultra-long phase-sensitive OTDR with hybrid distributed amplification," *Optics Letters*, 2014, 39(20): 5866.

[19] G. Cedilnik, G. Lees, P. E. Schmidt, S. Herstrom, and T. Geisler, "Pushing the reach of fiber distributed acoustic sensing to 125 km without the use of amplification," *IEEE Sensors Letters*, 2019, 3(3): 1–4.

[20] A. Masoudi and T. P. Newson, "High spatial resolution distributed optical fiber dynamic strain sensor with enhanced frequency and strain resolution," *Optics Letters*, 2017, 42(2): 290.

[21] X. Xiao, J. He, B. Du, B. Xu, G. Chen, X. Xu, *et al*., "High-spatial-resolution distributed acoustic sensor utilizing a positive- and negative-swept pulse," *Journal of Lightwave Technology*, 2024, 42(8): 2991–2996.

[22] T. M. Daley, D. E. Miller, K. Dodds, P. Cook, and B. M. Freifeld, "Field testing of modular borehole monitoring with simultaneous distributed acoustic sensing and geophone vertical seismic profiles at Citronelle, Alabama: field testing of MBM," *Geophysical Prospecting*, 2016, 64(5): 1318–1334.

[23] P. Jousset, T. Reinsch, T. Ryberg, H. Blanck, A. Clarke, R. Aghayev, *et al*., "Dynamic strain determination using fibre-optic cables allows imaging of seismological and structural features," *Nature Communications*, 2018, 9(1): 2509.

[24] A. Sladen, D. Rivet, J. P. Ampuero, L. De Barros, Y. Hello, G. Calbris, *et al*., "Distributed sensing of earthquakes and ocean-solid earth interactions on seafloor telecom cables," *Nature Communications*, 2019, 10(1): 5777.

[25] E. F. Williams, M. R. Fernández-Ruiz, R. Magalhaes, R. Vanthillo, Z. Zhan, M. González-Herráez, *et al*., "Distributed sensing of microseisms and teleseisms with submarine dark fibers," *Nature Communications*, 2019, 10(1): 5778.

[26] J. B. Ajo-Franklin, S. Dou, N. J. Lindsey, I. Monga, C. Tracy, M. Robertson, *et al*., "Distributed acoustic sensing using dark fiber for near-surface characterization and broadband seismic event detection," *Scientific Reports*, 2019, 9(1): 1328.

[27] S. Dou, N. Lindsey, A. M. Wagner, T. M. Daley, B. Freifeld, M. Robertson, *et al*., “Distributed acoustic sensing for seismic monitoring of the near surface: a traffic-noise interferometry case study,” *Scientific Reports*, 2017, 7(1): 11620.
[28] L. Xie, Z. Li, Y. Zhou, W. Xiang, Y. Wu, and Y. Rao, “Railway track online detection based on optical fiber distributed large-range acoustic sensing,” *IEEE Internet of Things Journal*, 2024, 11(4): 6469–6480.
[29] A. Masoudi, J. A. Pilgrim, T. P. Newson, and G. Brambilla, “Subsea cable condition monitoring with distributed optical fiber vibration sensor,” *Journal of Lightwave Technology*, 2019, 37(4): 1352–1358.
[30] L. Bouffaut, K. Taweesintananon, H. J. Kriesell, R. A. Rørstadbotnen, J. R. Potter, M. Landrø, *et al*., “Eavesdropping at the speed of light: distributed acoustic sensing of baleen whales in the arctic,” *Frontiers in Marine Science*, 2022, 9901348.
[31] M. Landrø, L. Bouffaut, H. J. Kriesell, J. R. Potter, R. A. Rørstadbotnen, K. Taweesintananon, *et al*., “Sensing whales, storms, ships and earthquakes using an arctic fibre optic cable,” *Scientific Reports*, 2022, 12(1): 19226.
[32] D. Rivet, B. De Cacqueray, A. Sladen, A. Roques, and G. Calbris, “Preliminary assessment of ship detection and trajectory evaluation using distributed acoustic sensing on an optical fiber telecom cable,” *The Journal of the Acoustical Society of America*, 2021, 149(4): 2615–2627.
[33] J. Chen, H. Li, T. Liu, C. Fan, Z. Yan, and Q. Sun, “Fully distributed hydroacoustic sensing based on lightweight optical cable assisted with scattering enhanced fiber,” in *2021 Optical Fiber Communications Conference and Exhibition (OFC)*, Washington, DC, 2021, pp. 1–3.
[34] G. Yan, D. Wang, J. Long, L. Jiang, Y. Gong, Z. Ran, *et al*., “High-performance towing cable hydrophone array with an improved ultra-sensitive fiber-optic distributed acoustic sensing system,” *Optics Express*, 2023, 31(16): 25545.
[35] A. Mateeva, J. Lopez, J. Mestayer, P. Wills, B. Cox, D. Kiyashchenko, *et al*., “Distributed acoustic sensing for reservoir monitoring with VSP,” *The Leading Edge*, 2013, 32(10): 1278–1283.
[36] G. Byerley, D. Monk, P. Aaron, and M. Yates, “Time-lapse seismic monitoring of individual hydraulic frac stages using a downhole DAS array,” *The Leading Edge*, 2018, 37(11): 802–810.
[37] G. Busanello, R. Bachrach, A. Sayed, and B. Soliman, “Surface distributed acoustic sensing for high-resolution near-surface characterization: results from a 3D onshore field experiment,” *Geophysics*, 2024, 89(2): KS39–KS51.
[38] J. Mestayer, B. Cox, P. Wills, D. Kiyashchenko, J. Lopez, M. Costello, *et al*., “Field trials of distributed acoustic sensing for geophysical monitoring,” *SEG Technical Program Expanded Abstracts 2011*, 2011(1): 4253–4257.
[39] G. Carvajal, M. Maucec, and S. Cullick, “*Intelligent Digital Oil and Gas Fields*,” 1st ed., Amsterdam: Elsevier, 2017.
[40] I. Ashry, Y. Mao, B. Wang, F. Hveding, A. Bukhamsin, T. K. Ng, *et al*., “A review of distributed fiber-optic sensing in the oil and gas industry,” *Journal of Lightwave Technology*, 2022, 40(5): 1407–1431.
[41] A. Mateeva, J. Lopez, H. Potters, J. Mestayer, B. Cox, D. Kiyashchenko, *et al*., “Distributed acoustic sensing for reservoir monitoring with vertical seismic profiling,” *Geophysical Prospecting*, 2014, 62(4): 679–692.
[42] B. S. Hart, “Definition of subsurface stratigraphy, structure and rock properties from 3-D seismic data,” *Earth – Science Reviews*, 1999, 47(3–4): 189–218.
[43] P. M. Shearer, “*Introduction to Seismology*,” Cambridge: Cambridge University Press, 2009.
[44] J. Han, W. Zhang, D. Jiang, Z. Wang, and F. Li, “Fiber optic 3-component seismometer,” *Photonic Sensors*, 2014, 4(2): 102–107.
[45] F. Liu, D. Yi, Y. Chen, P. Xu, M. Zhang, X. Zhu, *et al*., “Common-mode noise self-suppressed 3-component fiber optic accelerometer based on low-reflectivity Bragg gratings,” *Optics Letters*, 2021, 46(7): 1596.
[46] T. M. Daley, B. M. Freifeld, J. Ajo-Franklin, S. Dou, R. Pevzner, V. Shulakova, *et al*., “Field testing of fiber-optic distributed acoustic sensing (DAS) for subsurface seismic monitoring,” *The Leading Edge*, 2013, 32(6): 699–706.
[47] A. Bakulin, P. Golikov, R. Smith, K. Erickson, I. Silvestrov, and M. Al-Ali, “Smart DAS upholes for simultaneous and near-surface characterization and subsurface imaging,” *The Leading Edge*, 2017, 36(12): 1001–1008.
[48] B. Luo, W. Trainor-Guitton, E. Bozdağ, L. LaFlame, S. Cole, and M. Karrenbach, “Horizontally orthogonal distributed acoustic sensing array for earthquake- and ambient-noise-based multichannel analysis of surface waves,” *Geophysical Journal International*, 2020, 222(3): 2147–2161.
[49] B. N. Kuvshinov, “Interaction of helically wound fibre-optic cables with plane seismic waves: interaction of fibre-optic cables,” *Geophysical Prospecting*, 2016, 64(3): 671–688.
[50] J. C. Hornman, “Field trial of seismic recording using distributed acoustic sensing with broadside sensitive fibre-optic cables,” *Geophysical Prospecting*, 2017, 65(1): 35–46.
[51] I. L. C. Ning and P. Sava, “High-resolution multi-component distributed acoustic sensing,”

Geophysical Prospecting, 2018, 66(6): 1111–1122.
[52] D. Donno, B. Papp, A. Hartog, and J. Martin, "Fiber optic distributed vibration sensing with directional sensitivity," U.S. Patent 9880047, Jan. 30, 2018.
[53] A. H. Hartog, "*An Introduction to Distributed Optical Fibre Sensors*," Boca Raton: CRC Press, 2017.
[54] B. Han, H. Guan, J. Yao, Y. J. Rao, Z. Ran, Y. Gong, *et al*., "Distributed acoustic sensing with sensitivity-enhanced optical cable," *IEEE Sensors Journal*, 2021, 21(4): 4644–4651.
[55] A. Bona, T. Dean, J. Correa, R. Pevzner, K. V. Tertyshnikov, and L. Van Zaanen, "Amplitude and phase response of DAS receivers," in *79th EAGE Conference & Exhibition 2017*, Paris, 2017, pp. 1–5.
[56] H. F. Wang, X. Zeng, D. E. Miller, D. Fratta, K. L. Feigl, C. H. Thurber, *et al*., "Ground motion response to an ML 4.3 earthquake using co-located distributed acoustic sensing and seismometer arrays," *Geophysical Journal International*, 2018, 213(3): 2020–2036.